Supplementary Information

Mechanism and preparation research of binary heteroatoms co-doped (X=N,S,P) Platinum/carbon black electrocatalysts for an enhanced oxygen reduction reaction via one-pot pyrolysis method

Fengning Bai,[12] Yantong Zhang,[2] Dongyu Hou,[12] Jian Chen,[12] Fanming Meng,[12] Michael K.H. Leung,[3] Ling Zhou,[4] Yingjie Zhang,[2] Chengxu Zhang,[*12] Wutao Wang,[*5] and Jue Hu[*1]

1. Faculty of Metallurgical and Energy Engineering, Kunming University of Science and Technology, Kunming 650093, China. E-mail: chxzhang@kust.edu.cn
2. National and Local Joint Engineering Research Center for Lithium-ion Batteries and Materials Preparation Technology
3. Ability R&D Energy Research Centre, School of Energy and Environment, City University of Hong Kong, Hong Kong, China. E-mail: mkh.leung@cityu.edu.hk
4. City College，Kunming University of Science and Technology, Kunming 650093, China
5. LuXi KuoBo Precious Metals Co.,Ltd, Honghe, 651400, China. E-mail: 642329529@qq.com

Corresponding Author

*E-mail: chxzhang@kust.edu.cn

This file contains:

Supplementary Note 1: Materials

Carbon Black BP 2000 purchased from Cabot in the United States. Melamine (99%), Acetylacetone Platinum (97%), and Isopropanol purchased from Aladdin Reagent. Thiourea (99%) purchased from Tianjin Chemical Reagent Factory. Ammonium Dihydrogen Phosphate (99%) purchased from Ron Reagent. Anhydrous Ethanol (99%) purchased from Tianjin Fuyu Fine Chemical Co., Ltd. Concentrated Sulfuric Acid (98%) purchased from Chengdu Kolon Chemical. Concentrated Perchloric Acid (70.0%-72.0%) purchased from Tianjin Xinyuan Chemical. Nafion Solution (5.0 wt.%) purchased from DuPont in the United States. Commercial Pt/C catalyst (20%) purchased from Zhuangxin Wanfeng (Shanghai) Chemical Co., Ltd. Nano Al_2O_3 Polishing Powder (300nm/50nm, 99%) purchased from Tianjin Aidahengsheng Technology Development Co., Ltd. Ultra-pure water with a specific resistance of 18.25MΩ was used. All chemicals were used as received without further treatment.

Supplementary Note 2: Catalyst preparation

Firstly, 50 mg of BP 2000 and 10 mg of $Pt(acac)_2$ were accurately weighed and placed in a mortar, followed by manual grinding for 10 minutes to ensure thorough mixing. Subsequently, the mixture was transferred into a crucible with a conical shape alumina boat and subjected to a pyrolysis treatment at 900°C in a tube furnace under an argon atmosphere, with a heating rate of 5°C/min. After 1 hour of pyrolysis, the obtained catalyst was returned to the mortar for further grinding, resulting in the final catalyst powder named Pt/BP-900-10%. For the preparation of Pt/BP-N catalyst, the same procedure was followed with the addition of 250 mg of melamine during the weighing process, while keeping the remaining steps consistent, yielding the catalyst Pt/BP-N_{250}. In this process, the pyrolysis temperature (700°C-1000°C), $Pt(acac)_2$ loading amount (10%-40% Pt loading), and melamine addition amount (100 mg, 250 mg, 500 mg) were considered as variables. Firstly, the influence of pyrolysis temperature on the electrochemical performance of the catalyst was investigated, followed by studying the effect of Pt loading on the electrochemical performance of the catalyst. Finally, the impact of different N doping levels on the electrochemical performance of the catalyst was explored. The preparation method for Pt/BP-S (P) catalysts was similar to Pt/BP-N, with the exception that thiourea or ammonium dihydrogen phosphate was used instead of melamine, resulting in catalysts Pt/BP-S (Pt/BP-P). Similarly, there were three variables: pyrolysis temperature, Pt loading amount, and S (P) doping level.

The experimental procedure for the co-doped catalyst series is similar to that of the single-atom catalysts, with the difference being the addition of dual dopants instead of a single dopant. Firstly, the doping amounts of N (melamine) and S (thiourea) as well as the Pt loading amount were fixed, and temperature optimization was conducted. The temperatures were set at 700°C, 800°C, 900°C, and 1000°C, respectively. This resulted in catalysts Pt/BP-$N_{250}S_{250}$-700-10%, Pt/BP-$N_{250}S_{250}$-800-10%, Pt/BP-$N_{250}S_{250}$-900-10%, and Pt/BP-$N_{250}S_{250}$-1000-10%. From these, the pyrolysis temperature with the best electrochemical performance (900°C) was chosen for Pt loading optimization, with loading amounts of 10%, 20%, 30%, and 40%. This yielded catalysts Pt/BP-$N_{250}S_{250}$-900-10%, Pt/BP-$N_{250}S_{250}$-900-20%, Pt/BP-$N_{250}S_{250}$-900-30%, and Pt/BP-$N_{250}S_{250}$-900-40%. Subsequently, the Pt loading amount of the catalyst with the best electrochemical performance was selected for the optimization of N and S doping amounts (melamine and thiourea addition amounts). This resulted in catalysts Pt/BP-$N_{100}S_{250}$-900-30%, Pt/BP-$N_{250}S_{100}$-900-30%, Pt/BP-$N_{250}S_{500}$-900-30%, and Pt/BP-$N_{500}S_{250}$-900-30%. By replacing the S source (thiourea) with a P source (ammonium dihydrogen phosphate) while keeping the N source unchanged, the remaining optimization steps remained the same, except for setting the Pt loading amounts to 5%, 10%, 20%, and 30%. This yielded the Pt/BP-NP series of catalysts. Similarly, by replacing the N source (melamine) with a P source (ammonium dihydrogen phosphate) while keeping the S source unchanged, the remaining optimization steps remained the same, resulting in the Pt/BP-SP series of catalysts.

Supplementary Note 3: Catalyst characterization

All X-ray diffraction (XRD) patterns of the samples in this study were obtained using an Empyrean instrument from PANalytical, Netherlands. XRD analysis was primarily employed to investigate the composition, internal structure, and morphology of the catalyst samples. Cu-Kα radiation was utilized with an energy of 40 kV, scanning angles ranging from 10° to 90°, and a scanning rate of 5°/min. Transmission electron microscopy (TEM) measurements were conducted using a JEM-F200 instrument from Japan. The sample preparation involved dispersing a portion of the sample in ethanol solution through ultrasonication. Subsequently, a few drops of the dispersed liquid were transferred onto a microgrid copper mesh using a 10 µl pipette. After air drying, the sample was placed in the instrument and imaged at an acceleration voltage of 200 kV to capture high-resolution morphological details and particle size. Elemental mapping was performed using the energy-dispersive X-ray spectroscopy (EDS) attachment on the TEM. X-ray photoelectron spectroscopy (XPS) analysis was carried out using an XPS instrument from ThermoFisher, USA. The analysis chamber was maintained at a vacuum level of $4*10^{-9}$ mbar. Al Kα radiation (hv=1486.6 eV) was used as the excitation source with a working voltage of 14.6 kV and a filament current of 13.5 mA. Signal accumulation was performed over 20 cycles, and the data were collected with a passing energy of 20 eV and a step size of 0.1 eV. Charging correction was performed with respect to the C 1s=284.8 eV binding energy as the energy reference. Raman spectroscopy was conducted using a LabRAM Odyssey Raman spectrometer produced in France. The radiation source had a wavelength of 532 nm and was primarily employed to evaluate the graphitization degree and carbon defect density in the catalyst materials. The specific surface area of the samples, determined using the Brunauer-Emmett-Teller (BET) method, was measured using a Quantachrome NOVA 2000 surface and pore analyzer from Quantachrome Instruments, USA. Prior to testing, the catalysts underwent N_2 pretreatment, and the analysis was conducted at 77.35 K using a nitrogen adsorption-desorption instrument. Inductively coupled plasma (ICP) analysis was performed using an Agilent 5110 instrument manufactured by Agilent Technologies (China) Pty Ltd., Australia. The sample preparation involved weighing 10 mg of the catalyst and adding 20 ml of freshly prepared aqua regia (5 ml concentrated nitric acid + 15 ml concentrated hydrochloric acid) to a beaker. The mixture was stirred overnight, and the solution was then filtered, washed, and collected. The filtrate was transferred to a 100 ml volumetric flask, diluted to volume, and finally, 10 ml of the solution was directly analyzed.

Supplementary Note 4: Electrochemical measurements

All electrochemical tests conducted in this study were performed using a three-electrode system with a CHI 760E electrochemical workstation. The three-electrode system consisted of: (1) a reference electrode of Ag/AgCl (with a salt bridge saturated with potassium chloride (KCl) solution); (2) a platinum foil as the counter electrode, measuring 2 cm × 2 cm in size; (3) a glassy carbon electrode as the working electrode. For rotating disk electrode (RDE) testing, the electrode had a diameter of 0.5 cm and an area of 0.19625 cm^2, while for rotating ring-disk electrode (RRDE) testing, the electrode had a diameter of 0.6 cm and an area of 0.2826 cm^2. The electrolytes used in our experiments were 0.5 M H_2SO_4 and 0.1 M $HClO_4$. Additionally, in this study, all electrode potentials were converted to the standard reversible hydrogen electrode (RHE) potential by using hydrogen calibration. Since the potential of Ag/AgCl electrode after hydrogen calibration was 0.212 V, the conversion formula used was: E(V vs. RHE) = E(Ag/AgCl) + 0.212 V. All electrochemical measurements were conducted at atmospheric pressure and a temperature of 30°C, controlled by a digital constant temperature oil bath stirrer.

To prepare the catalyst ink, a 5 wt.% Nafion solution was diluted with isopropanol to obtain a 0.5 wt.% Nafion/isopropanol solution. Then, 5 mg of the pre-ground catalyst was placed in a 3 ml sample bottle, and 200 µl of isopropanol, 200 µl of 0.5 wt.% Nafion/isopropanol solution, and 100 µl of ultrapure water were added. The mixture was sonicated for at least 1 hour to achieve a homogeneous catalyst dispersion. Prior to formal testing, the RDE and RRDE electrodes were polished by drawing an "8" pattern on chamois with nano Al_2O_3 polishing powder mixed with water. This process removed impurities and scratches from the electrode surface. The electrodes were then cleaned by ultrasonicating them in water. A suitable volume of the prepared catalyst ink was pipetted onto the RDE or RRDE electrodes, taking care to avoid droplets outside the electrode area. The ink was allowed to air dry. The theoretical Pt loading of the prepared catalyst on the electrode was 80 μg_{Pt} cm^{-2}, while the commercial Pt/C catalyst used for comparison had a Pt loading of 60 μg_{Pt} cm^{-2} on the electrode.

The electrochemical performance of the prepared catalysts for oxygen reduction reaction (ORR) was evaluated using the CHI 760E electrochemical workstation. RDE measurements were conducted to perform cyclic voltammetry (CV), linear sweep voltammetry (LSV), and stability tests. RRDE measurements were carried out to determine the electron transfer number (n) and hydrogen peroxide yield (H_2O_2%). CV curves at a scan rate of 50 mV s^{-1} and LSV curves at a scan rate of 5 mV s^{-1} were separately recorded in electrolytes saturated with N_2 and O_2. For LSV measurements in O_2-saturated electrolyte, the RDE was rotated at 1600 rpm, while for N_2-saturated electrolyte, the RDE was kept stationary as the baseline. LSV curves were obtained at different rotation speeds of 2500, 2025, 1600, 1025, 900, 625, and 400 rpm, and the Koutecky-Levich equation (Eq. 1) was used to calculate the kinetic current density (J_k) based on the curves.

$$\frac{1}{J}=\frac{1}{J_l}+\frac{1}{J_k}=\frac{1}{B\omega^{1/2}}+\frac{1}{J_k}\quad\left(B = 0.62nFC_0D_0^{2/3}\frac{1}{v^{1/6}}\right) \qquad (1)$$

In the equation, J represents the measured current density, J_l is the diffusion-limited current density, J_k is the kinetic current density, ω is the angular velocity, n is the electron transfer number, F is the Faraday constant (96485 mol^{-1}), C_0 is the volume concentration of O_2, D_0 is the diffusion coefficient of O_2, and v is the viscosity of the electrolyte.

RRDE testing was performed using a glassy carbon electrode with a Pt ring. The testing was

conducted in an O_2-saturated electrolyte while rotating the RRDE at 1600 rpm. From the obtained data, the electron transfer number (n) and hydrogen peroxide yield (H_2O_2%) during the ORR process were calculated using the following formulas. (Eq. 2 and Eq. 3)

$$H2O2\% = 200\frac{I_r}{NI_d + I_r} \quad (2)$$

$$n = 4I_d\frac{1}{I_d + I_r\frac{1}{N}} \quad (3)$$

Where I_r represents the ring current, I_d represents the disk current, and N represents the current collection efficiency of the ring electrode (N=0.37).

Electrochemically active surface area (ECSA) refers to the active surface area of the electrode participating in electrochemical reactions. The mass activity (MA) depends largely on the particle size of the electrocatalyst (i.e., the number of active sites), while the specific activity (SA) represents the current density per unit mass of catalyst on the unit ECSA. The calculation formulas are as follows. (Eq. 4, Eq. 5, and Eq. 6)

$$ECSA = S\frac{1}{0.21Vm_{Pt}} \quad (4)$$

$$MA = \frac{r_f J_k}{m} \quad (5)$$

$$SA = \frac{MA}{ECSA} \quad (6)$$

Where S represents the integrated charge area corresponding to the H desorption peak after the double-layer is subtracted, V is the scan rate, m_{Pt} is the mass of Pt on the working electrode, rf represents the roughness factor, which is the ratio of the true surface area of the catalyst to the geometric surface area of the working electrode, J_k represents the kinetic current density, and m is the areal mass loading of Pt in the catalyst on the electrode.

To evaluate the stability of the catalysts in 0.5 M H_2SO_4 during ORR, their performance was initially assessed by LSV, followed by cyclic voltammetry (CV) in the voltage range of 0.5 V to 0.7 V at a scan rate of 50 mV s^{-1}. We have made a comparison of commercial JM 20% Pt/C and Pt/BP-N250S250-900-30% in with HClO4 and H2SO4 conditions. As shown in Figure S18, we found the ORR performance of commercial 20% Pt/C in HClO4 is better than H2SO4, namely the E1/2 are 0.813V vs.0.785V (vs. RHE). However, for our catalysts, it shows a convert results. The performance measured in perchloric acid was slightly inferior to that measured in sulfuric acid (the half-wave potential of Pt/BP-N250S250-900-30% in 0.1M H2SO4 was 0.821 V vs. RHE, while in 0.1M HClO4 it was 0.739 V vs. RHE). This may be the reason of the unique structure of our catalysts. Subsequently, the LSV was performed again to evaluate the performance after 5000 cycles. The stability of the catalyst was assessed by comparing the changes in the LSV curves before and after the cycling. A smaller change indicates better catalyst stability.

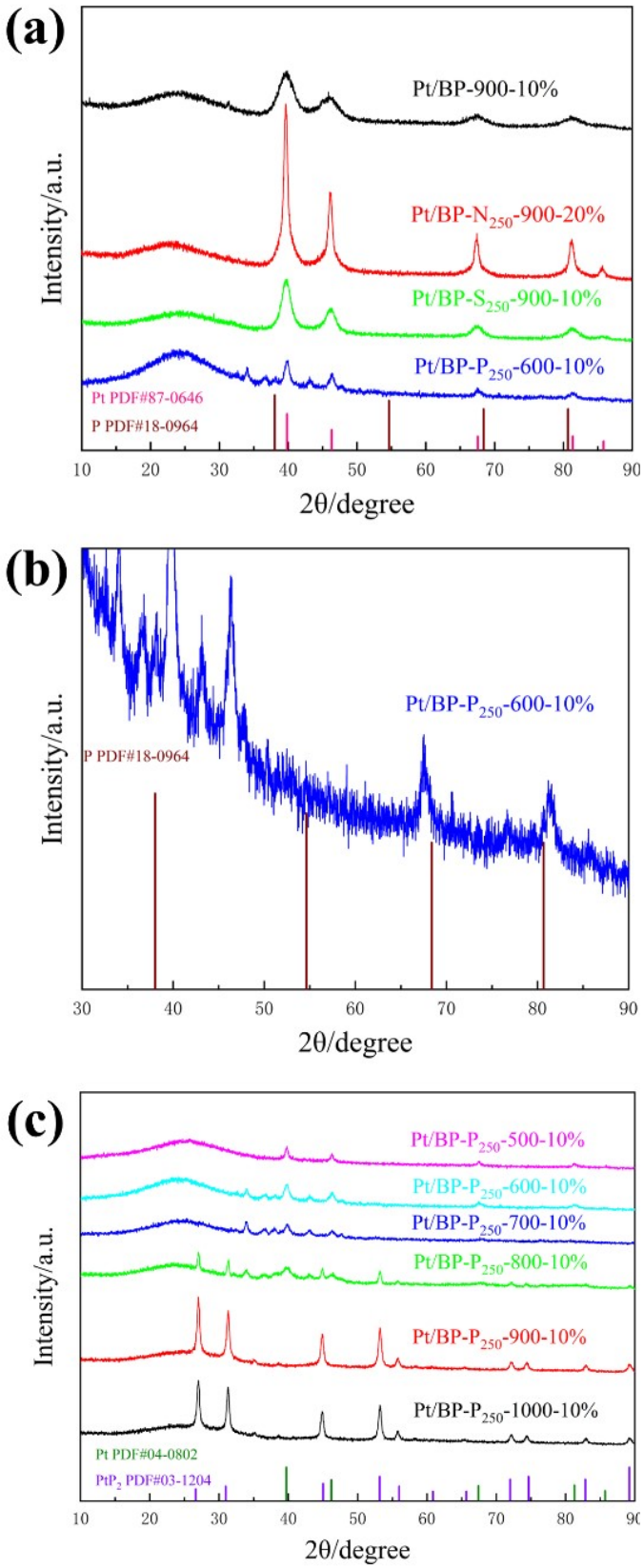

Supplementary Fig. 1 (a) XRD patterns of catalysts Pt/BP-900-10%, Pt/BP-N_{250}-900-20%, Pt/BP-S_{250}-900-10% and Pt/BP-P_{250}-900-10%; (b) Partial magnification of Pt/BP-P_{250}-900-10% XRD pattern; (b) XRD patterns of Pt/BP-P_{250}-10% series catalysts

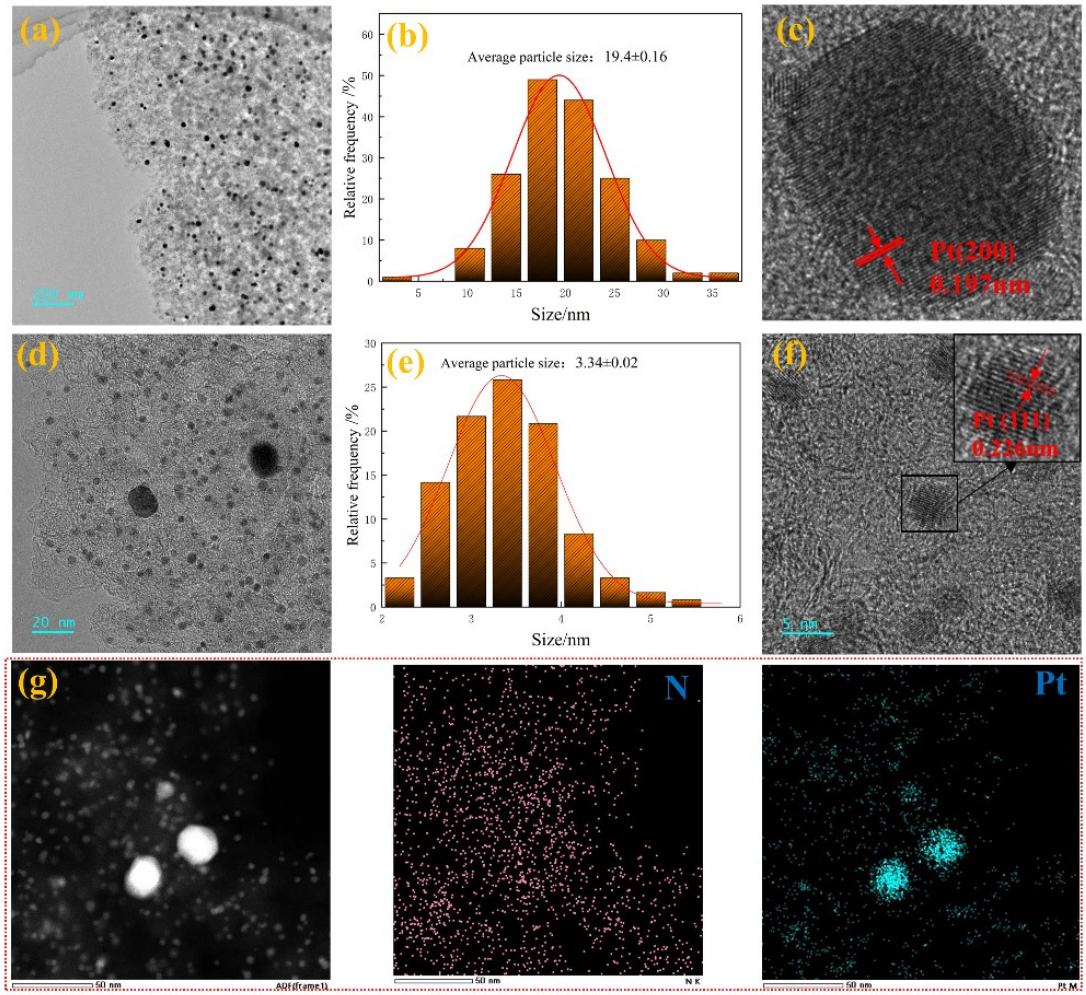

Supplementary Fig. 2 TEM, particle size distribution and EDS element mapping of Pt/BP-N_{250}-900-20% catalyst at different magnifications

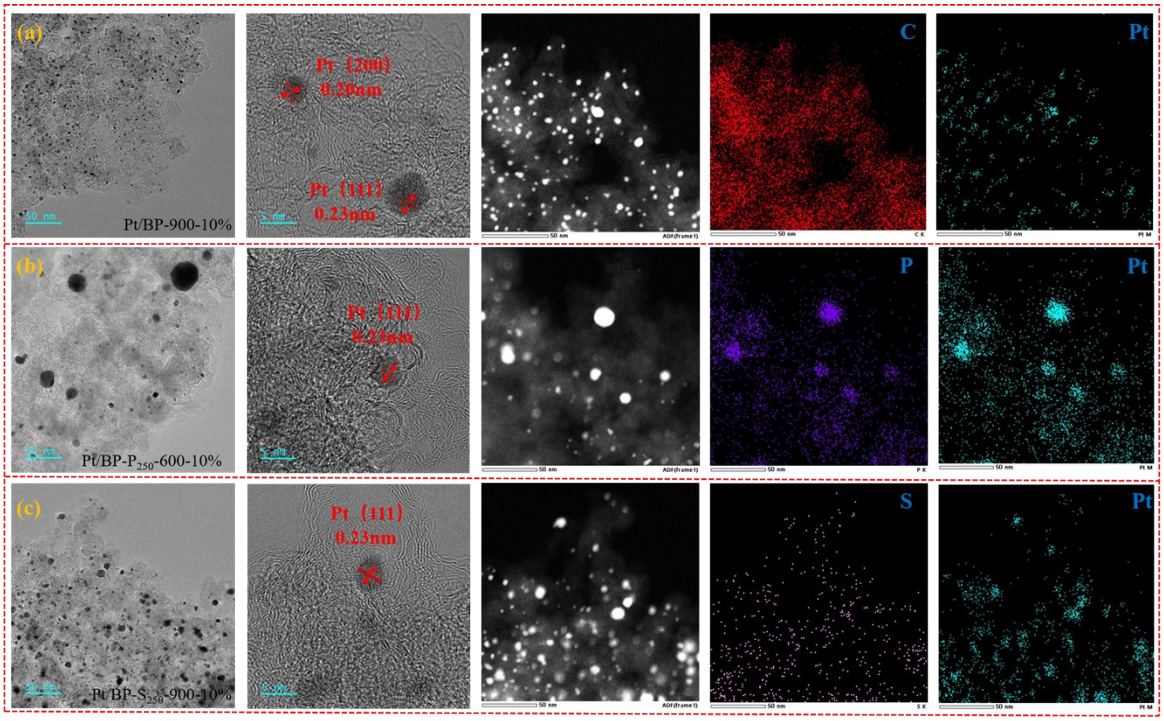

Supplementary Fig. 3 (a) TEM and EDS mapping of Pt/BP-900-10% catalyst; (b) TEM and EDS mapping of Pt/BP-P_{250}-600-10% catalyst; (c) TEM and EDS mapping of Pt/BP-S_{250}-900-10% catalyst

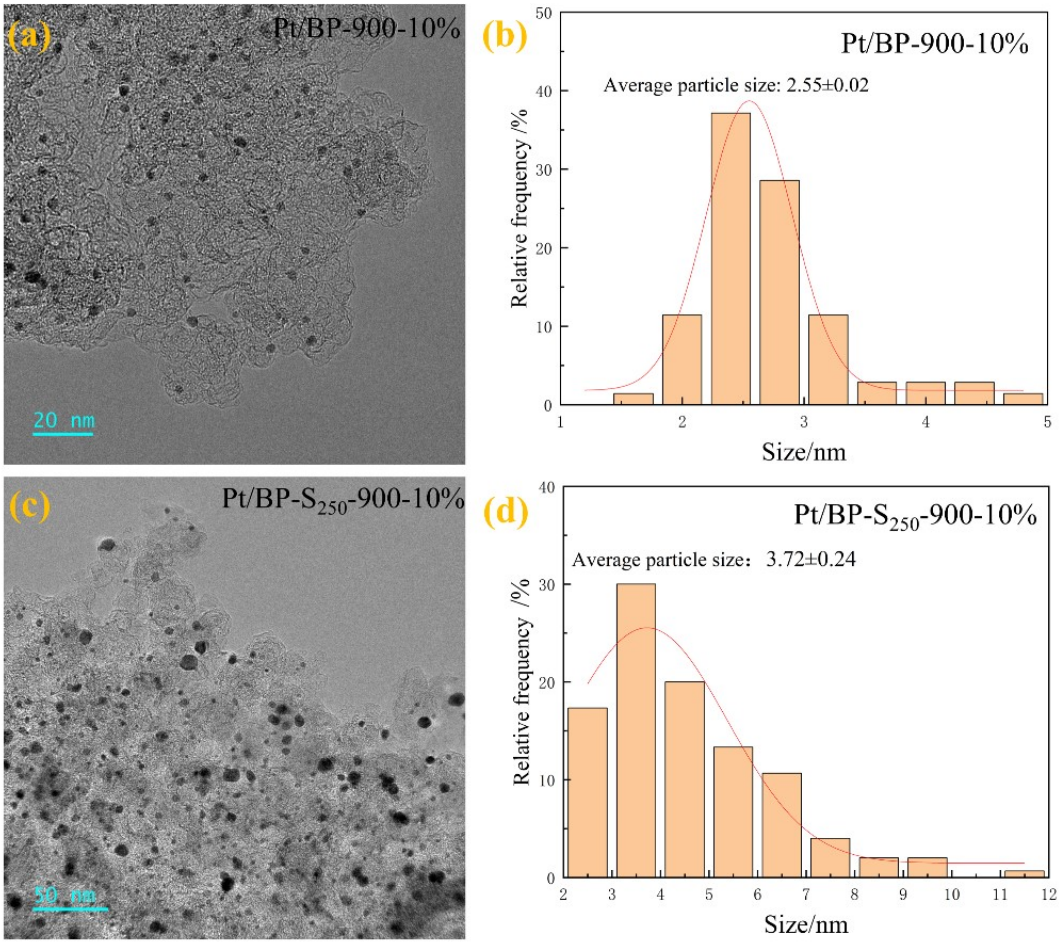

Supplementary Fig. 4 (a) TEM diagram of Pt/BP-900-10% catalyst and its particle size distribution; (c, d) TEM diagram of Pt/BP-S_{250}-900-10% catalyst and its particle size distribution

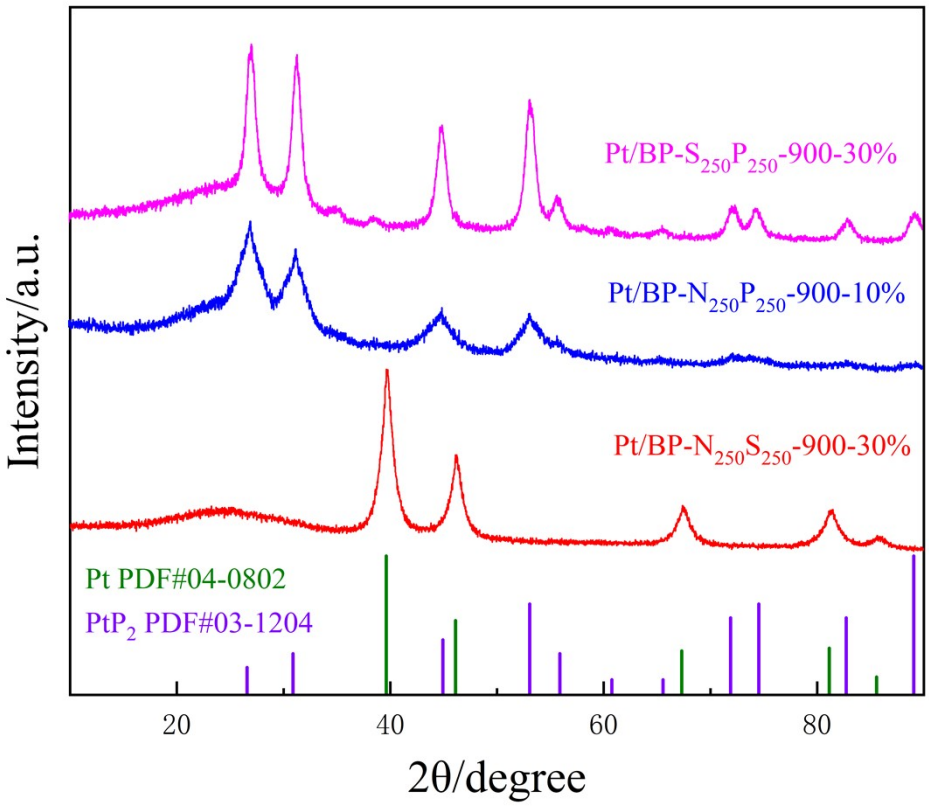

Supplementary Fig. 5 XRD patterns of catalysts Pt/BP-$N_{250}S_{250}$-900-30%, Pt/BP-$N_{250}P_{250}$-900-10% and Pt/BP-$S_{250}P_{250}$-900-30%

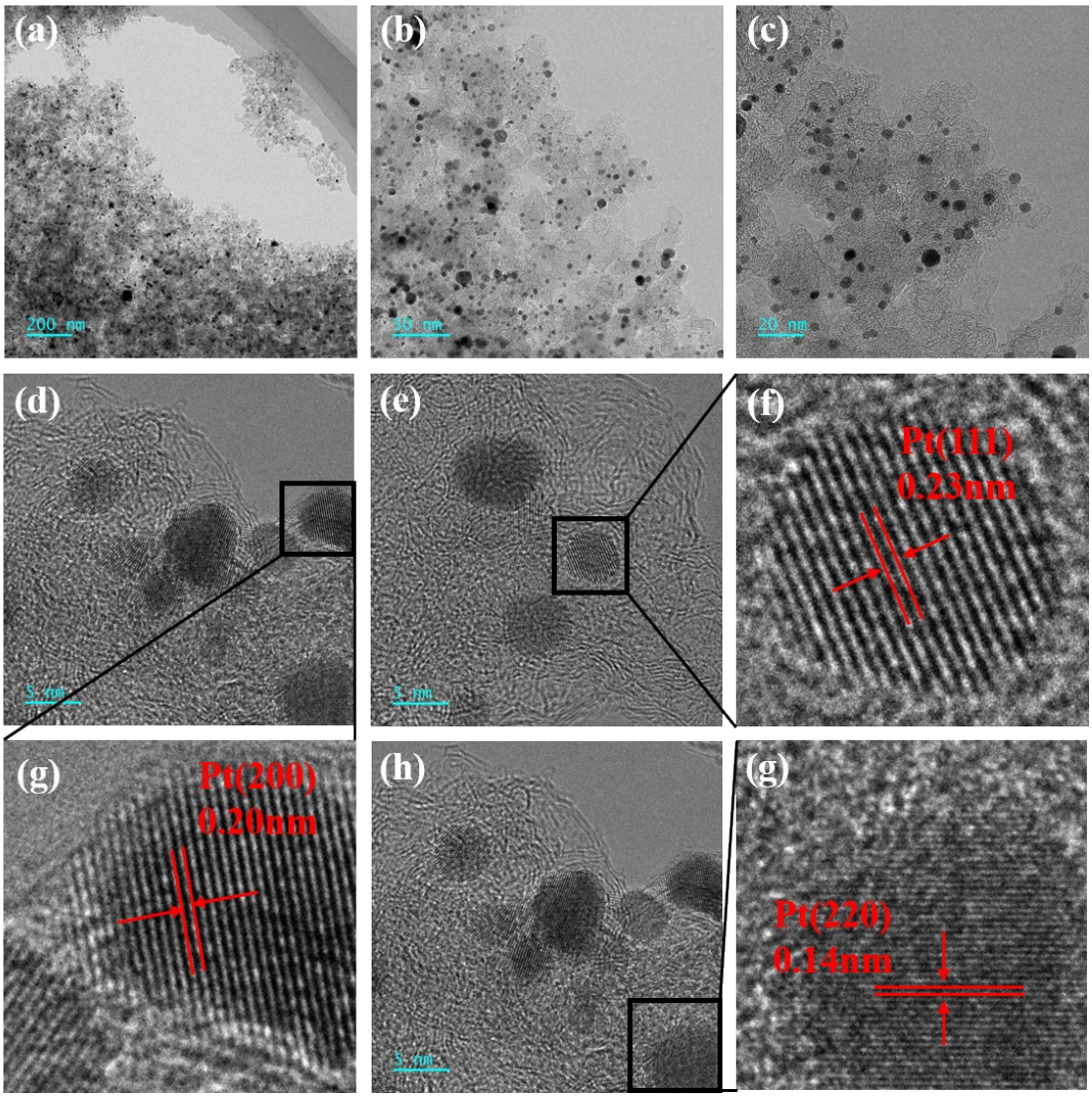

Supplementary Fig. 6 TEM image (a-c) of Pt/BP-$N_{250}S_{250}$-900-30% catalyst at different magnifications; (d-g) HAADF-STEM images

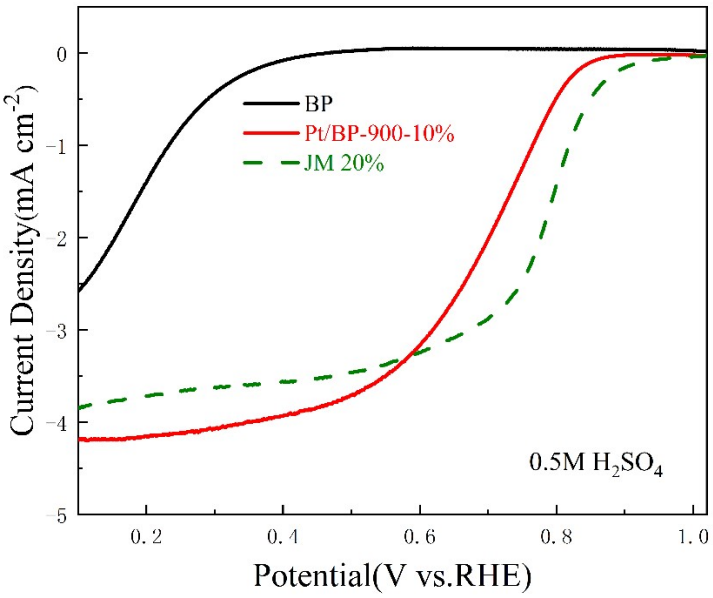

Supplementary Fig. 7 Comparison of LSV curves of pure BP, Pt/BP-900-10% and commercial Pt/C

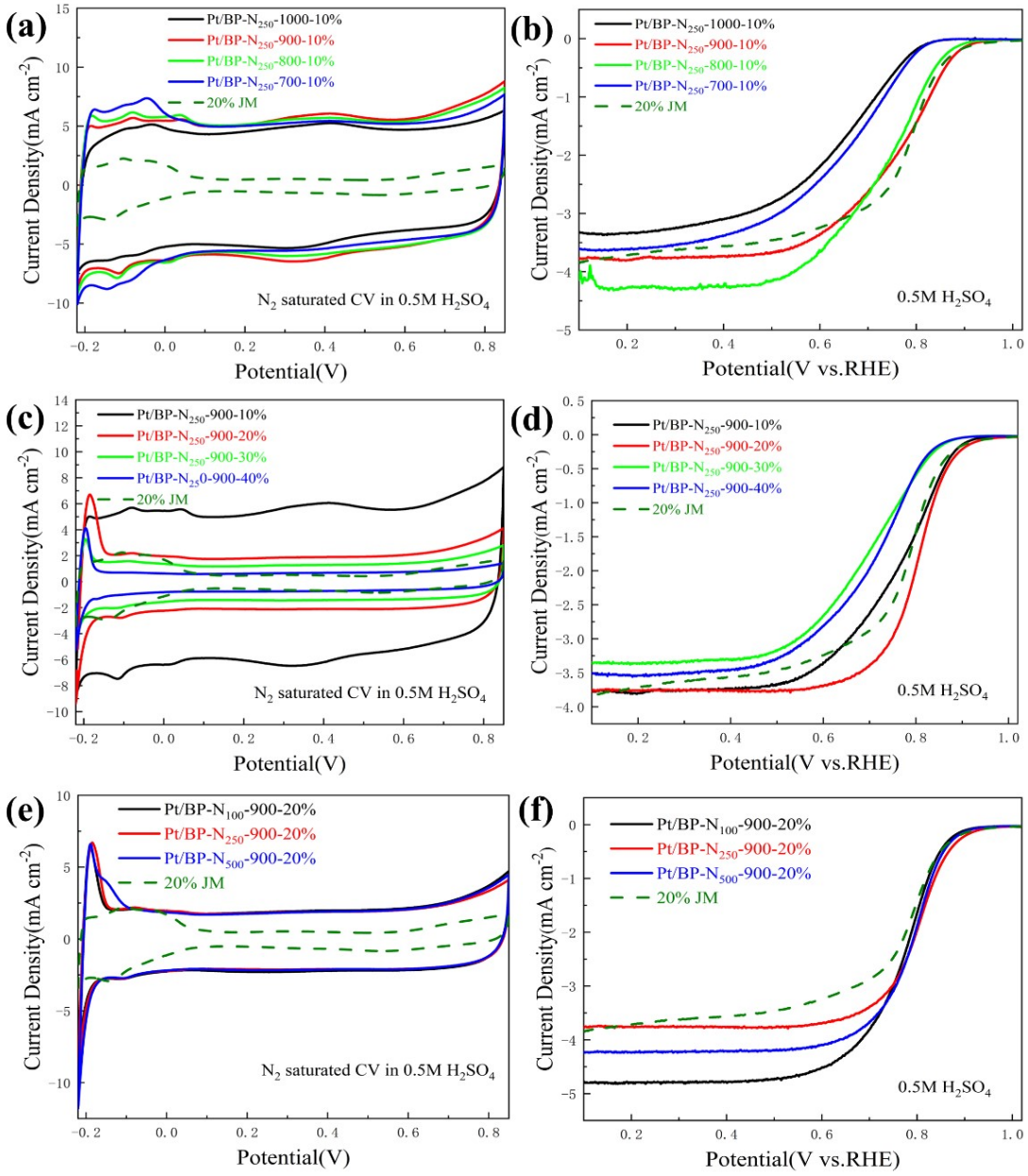

Supplementary Fig. 8 CV diagram under N_2 saturation and LSV diagram under O_2 saturation; (a, b) Comparison diagram of temperature optimization performance of Pt/BP-N series catalysts; (c, d) Comparison diagram of optimization performance of Pt/BP-N series catalysts with Pt load; Comparison of the performance of (e, f) Pt/BP-N series catalysts with N doping amount

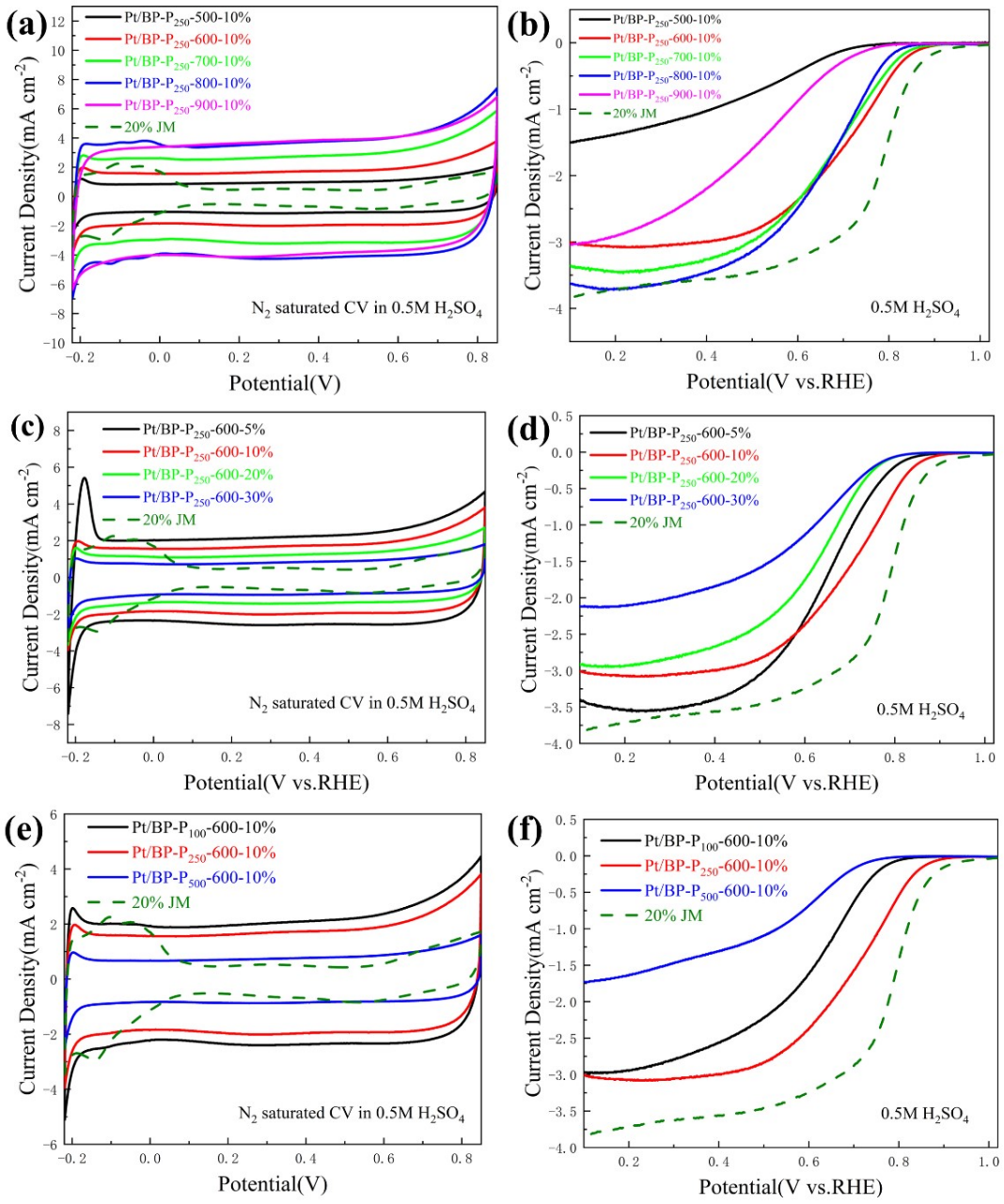

Supplementary Fig. 9 CV diagram under N_2 saturation and LSV diagram under O_2 saturation; (a, b) Comparison diagram of temperature optimization performance of Pt/BP-P series catalysts; (c, d) Comparison diagram of optimization performance of Pt/BP-P series catalysts with Pt load; Comparison of the performance of (e, f) Pt/BP-P series catalysts with N doping amount

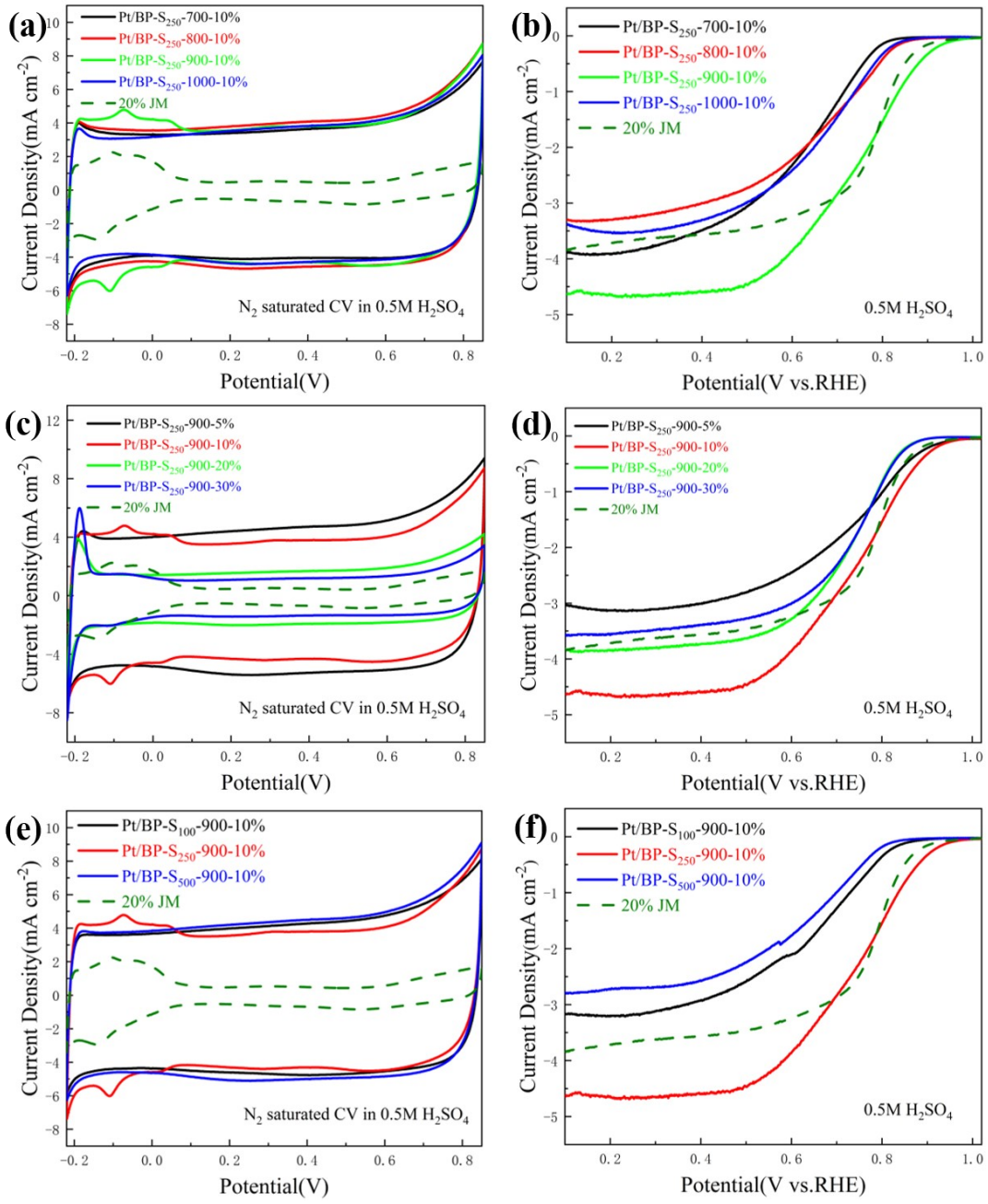

Supplementary Fig. 10 CV diagram under N_2 saturation and LSV diagram under O_2 saturation; (a, b) Comparison diagram of temperature optimization performance of Pt/BP-S series catalysts; (c, d) Comparison diagram of optimization performance of Pt/BP-S series catalysts with Pt load; Comparison of the performance of (e, f) Pt/BP-S series catalysts with N doping amount

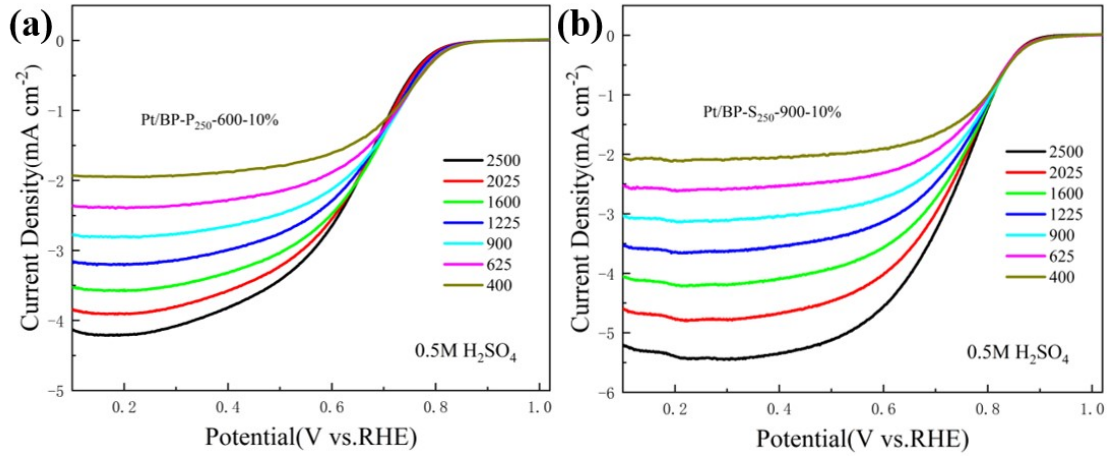

Supplementary Fig. 11 (a) LSV curves of sample Pt/BP-P_{250}-900-10% at different speeds; (b) LSV curves of sample Pt/BP-S_{250}-900-10% at different speeds

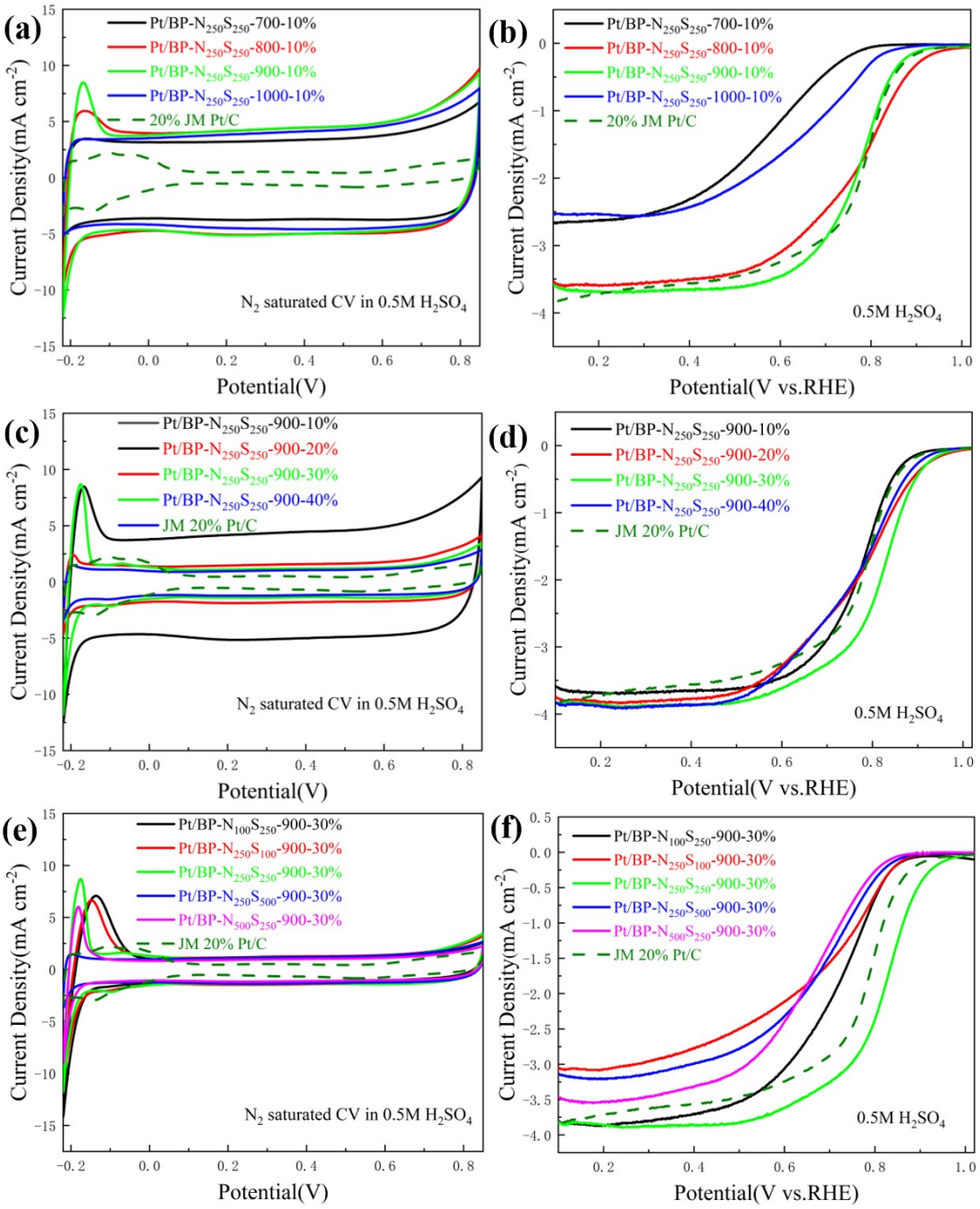

Supplementary Fig. 12 CV diagram under N_2 saturation and LSV diagram under O_2 saturation; (a, b) Comparison diagram of temperature optimization performance of Pt/BP-NS series catalysts; (c, d) Comparison diagram of optimization performance of Pt/BP-NS series catalysts with Pt load; Comparison of the performance of (e, f) Pt/BP-NS series catalysts with N and S doping amount

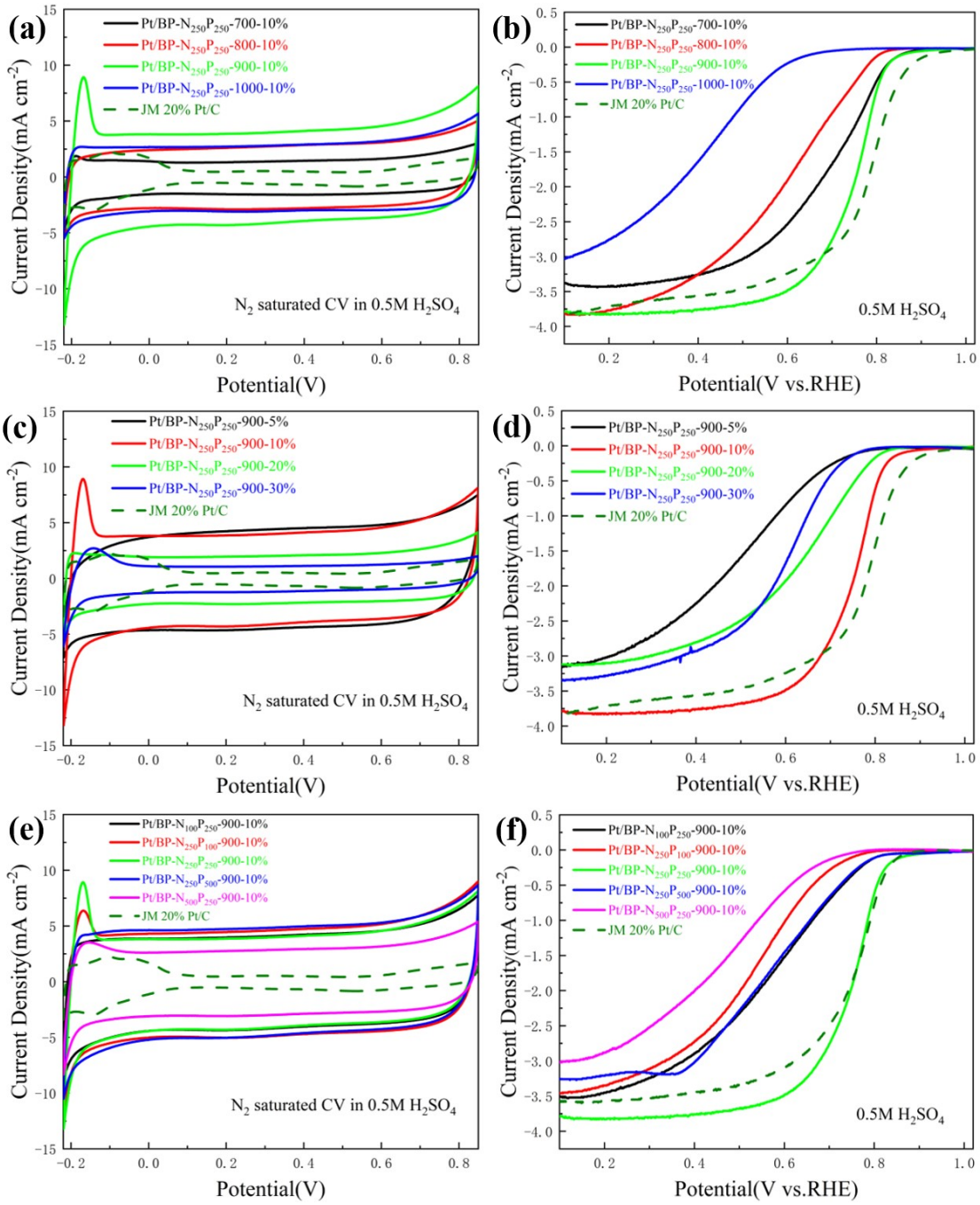

Supplementary Fig. 13 CV diagram under N_2 saturation and LSV diagram under O_2 saturation; (a, b) Comparison diagram of temperature optimization performance of Pt/BP-NP series catalysts; (c, d) Comparison diagram of optimization performance of Pt/BP-NP series catalysts with Pt load; Comparison of the performance of (e, f) Pt/BP-NP series catalysts with N and P doping amount

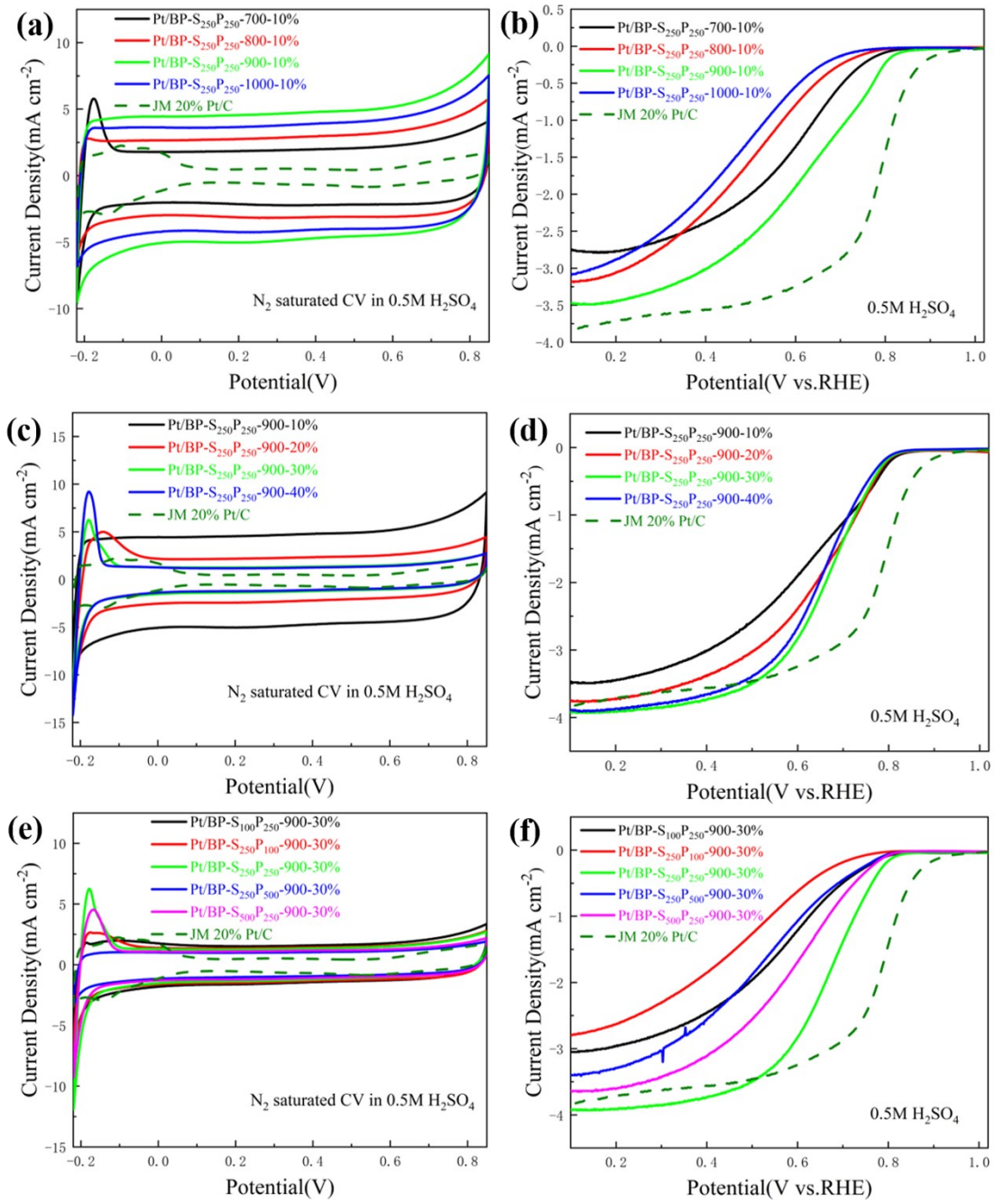

Supplementary Fig. 14 CV diagram under N_2 saturation and LSV diagram under O_2 saturation; (a, b) Comparison diagram of temperature optimization performance of Pt/BP-SP series catalysts; (c, d) Comparison diagram of optimization performance of Pt/BP-SP series catalysts with Pt load; Comparison of the performance of (e, f) Pt/BP-SP series catalysts with S and P doping amount

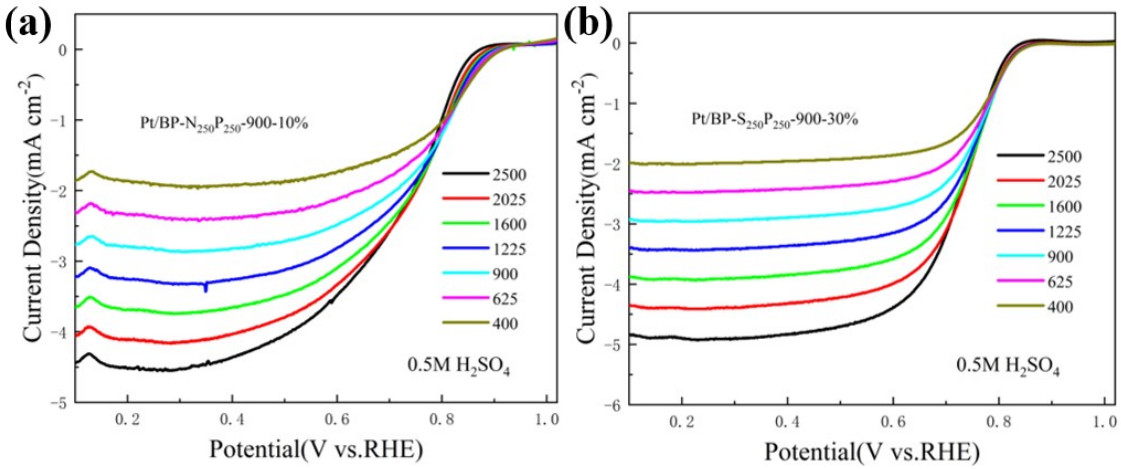

Supplementary Fig. 15 (a) LSV curves of catalyst Pt/BP-$N_{250}P_{250}$-900-10% at different speeds; (b) LSV curves of catalyst Pt/BP-$S_{250}P_{250}$-900-30% at different speeds

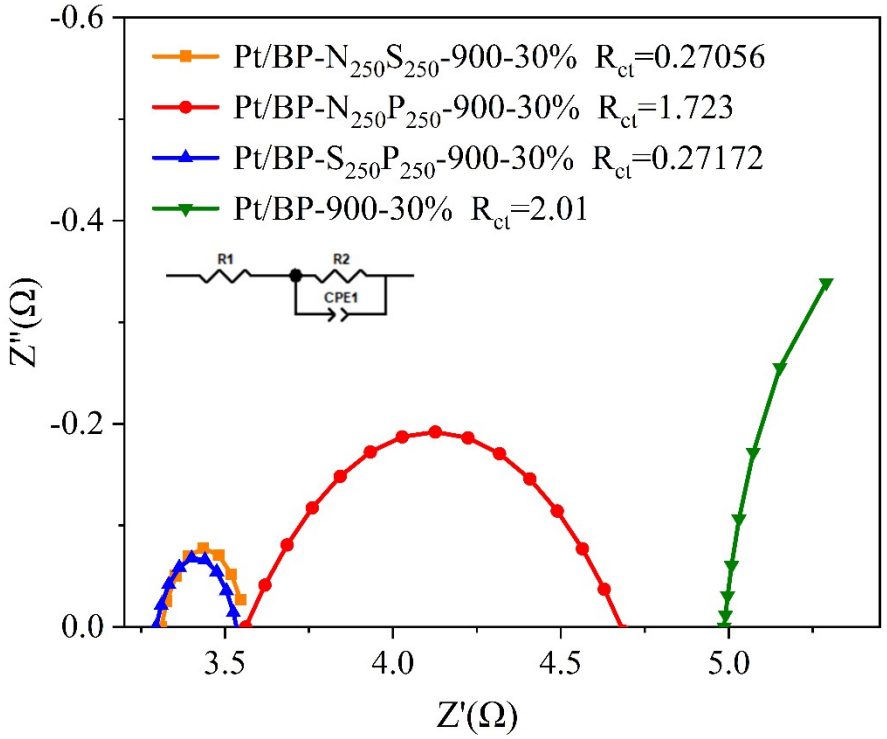

Supplementary Fig. 16 (a) EIS test chart of catalyst Pt/BP-$N_{250}P_{250}$-900-30%, Pt/BP-$N_{250}S_{250}$-900-30%, Pt/BP-$S_{250}P_{250}$-900-30% and Pt/BP-900-30%.

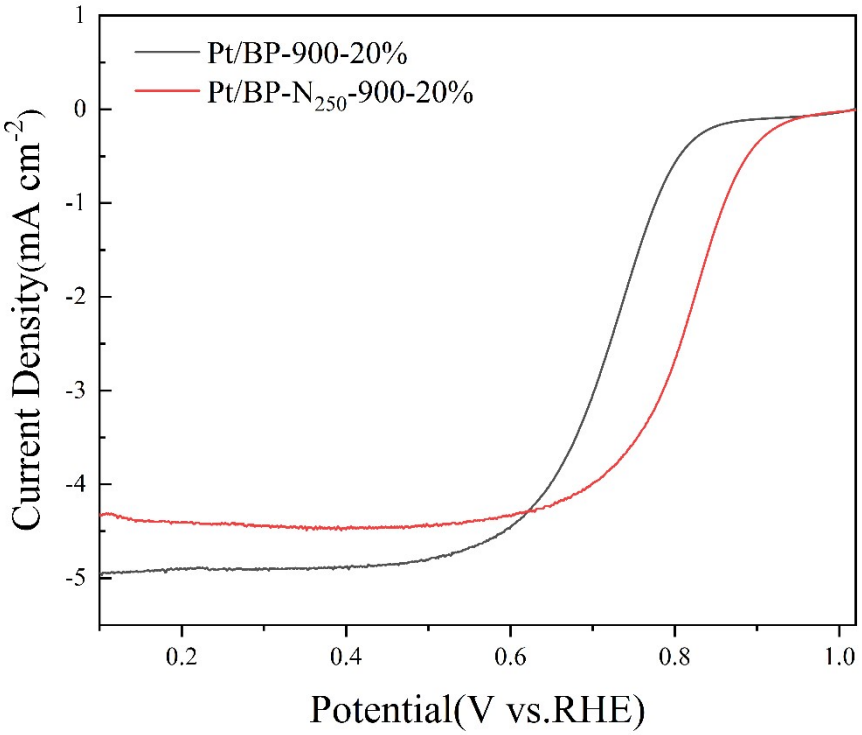

Supplementary Fig. 17 (a) LEV curves of catalyst Pt/BP-N_{250}-900-20% and Pt/BP-900-20%.

Samples	Pt content in ICP results	Half-wave potential $E_{1/2}$
Pt/BP-900-20%	14.46%	0.722 V vs. RHE
Pt/BP-N_{250}-900-20%	13.96%	0.803 V vs. RHE

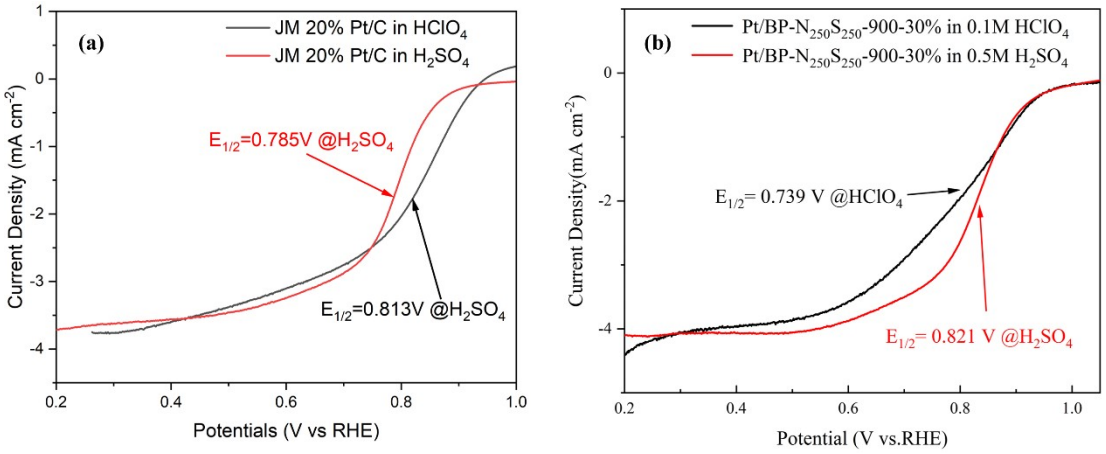

Supplementary Fig. 18 (a) LSV curves of commercial JM 20% Pt/C catalyst in 0.1M $HClO_4$ and 0.5M H_2SO_4; (b) LSV curves of commercial JM 20% Pt/C catalyst in 0.1M $HClO_4$ and 0.5M H_2SO_4.

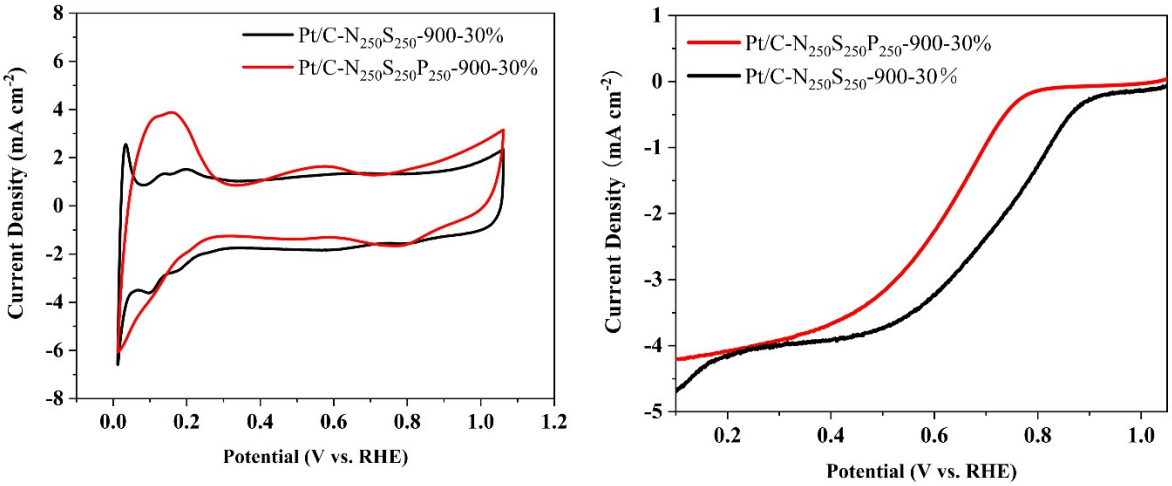

Supplementary Fig. 19 (a) LSV curves of catalyst Pt/BP-$N_{250}S_{250}$-900-30% and Pt/BP-$N_{250}S_{250}P_{250}$-900-30%; (b) CV curves of catalyst P Pt/BP-$N_{250}S_{250}$-900-30% and Pt/BP-$N_{250}S_{250}P_{250}$-900-30%.

Samples	Pt content in ICP results
Pt/BP-$N_{250}S_{250}$-900-30%	20.45%
Pt/BP-$N_{250}S_{250}P_{250}$-900-30%	25.15%

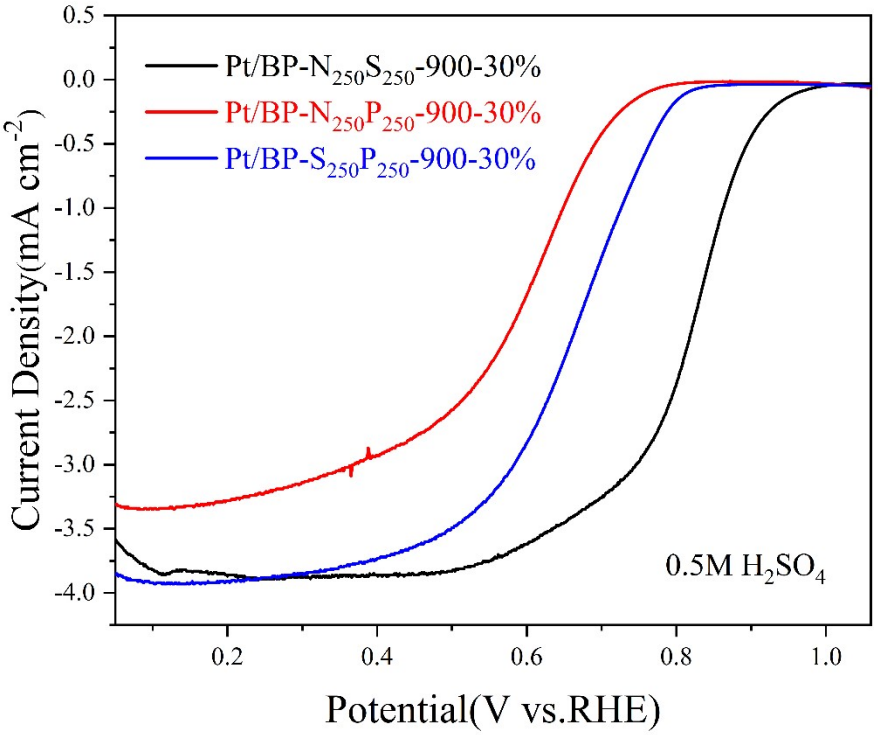

Supplementary Fig. 20 (a) LSV curves of catalyst Pt/BP-$N_{250}S_{250}$-900-30%, Pt/BP-$N_{250}P_{250}$-900-30% and Pt/BP-$S_{250}P_{250}$-900-30%;

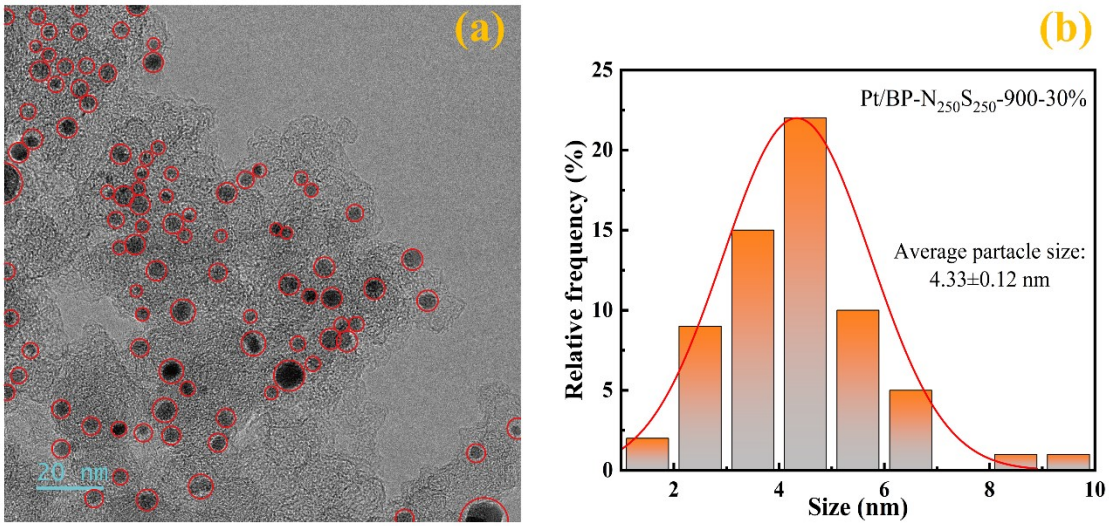

Supplementary Fig. 21 (a)TEM image of Pt/BP-$N_{250}S_{250}$-900-30% catalyst at different magnifications; (b) particle size distribution of Pt/BP-$N_{250}S_{250}$-900-30% catalyst;

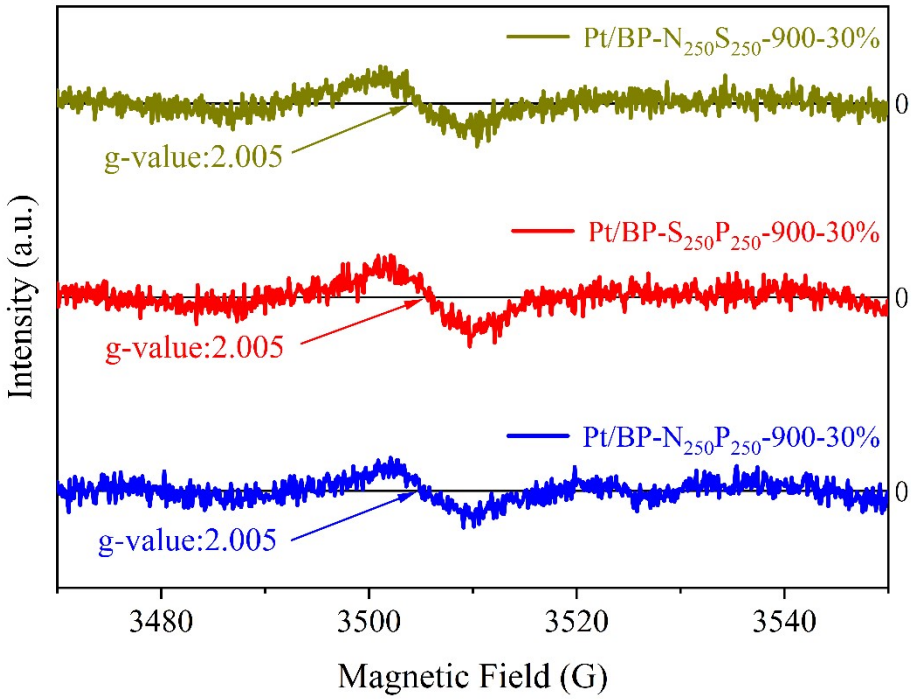

Supplementary Fig. 22 EPR spectra of Pt/BP-$N_{250}S_{250}$-900-30%, Pt/BP-$S_{250}P_{250}$-900-30% and Pt/BP-$N_{250}P_{250}$-900-30%

Supplementary Note 5: Computational details

All electronic structure calculations were performed using spin-polarized density functional theory (DFT) calculations implemented within the Vienna Ab initio Simulation Package (VASP)[1–4]. The projector augmented wave (PAW) potentials were employed to describe the interaction between valence electrons and ionic cores[5,6]. The generalized gradient approximation in the Perdew-Burke-Ernzerhof (PBE) form was used to describe the electronic exchange and correlation effects[7]. The wave function expansion at each k-point was carried out using a plane wave basis set with a dynamic cutoff energy of up to 550 eV. The Brillouin zone integration was approximated by summing over a special selection of k-points using the Monkhorst-Pack method[8], with a 2×2×1 grid. Thermodynamic corrections were applied using vaspkit[9,10]. Electronic occupancies were determined using a Gaussian broadening with a width of 0.05 eV. The geometrical structures were optimized until the energy convergence reached 1.0×10^{-5} eV/atom and the force convergence reached 0.05 eV/Å. For graphene-based structures, a supercell size of 12.33×10.67 Å and a vacuum layer thickness of 25 Å were used.

Based on our experimental observations, this study investigates the four-electron oxygen reduction reaction (ORR) mechanism in various graphene structures serving as theoretical computational models for carbon black microstructure. Under acidic conditions (PH=0), the ORR process can be summarized as follows:

$$* + O_2(g) + H^+ + e^- \rightarrow OOH * \quad (7)$$

$$OOH * + H^+ + e^- \rightarrow O * + H_2O \quad (8)$$

$$O * + H^+ + e^- \rightarrow OH * \quad (9)$$

$$OH * + H^+ + e^- \rightarrow * + H_2O * \quad (10)$$

For each individual step of the oxygen reduction reaction (ORR), the Gibbs free energy was calculated using the approach proposed by Nørskov et al[11] .The free energy change from the initial to the final state of the reaction is defined as follows:

$$G = E + \Delta E_{ZPE} - T\Delta S + \Delta G_U + \Delta G_{PH} \quad (11)$$

The symbols ΔE, ΔE_{ZPE}, and ΔS represent the total energy difference obtained from DFT calculations, the zero-point energy difference between the reactants and products, and the entropy difference, respectively. ΔG_U=eU, where U is the electrode potential with respect to standard hydrogen electrode, and e is the charge transferred. PH=0 for acid medium in this study. T represents the temperature (298.15K). The formula has been simplified using vaspkit501: $\Delta E=\Delta E_{ZPE}-T\Delta S+\Delta G_U$[12].

$$G = E + \Delta E + \Delta G_{PH} \quad (12)$$

The free energy changes for the four basic ORR steps can be obtained as follows: $\Delta G_1=G_{OOH*}$-4.92, $\Delta G_2=G_{O*}-G_{OOH*}$, $\Delta G_3=G_{OH*}-G_{O*}$, and $\Delta G_4=-G_{OH*}$. Therefore, the overpotential used to evaluate and ORR performance is applied according to the following equation:

$$\eta_{ORR} = \max(\Delta G_1, \Delta G_2, \Delta G_3, \Delta G_4)/e + 1.23 \quad (13)$$

where 1.23 represents the equilibrium potential[13].

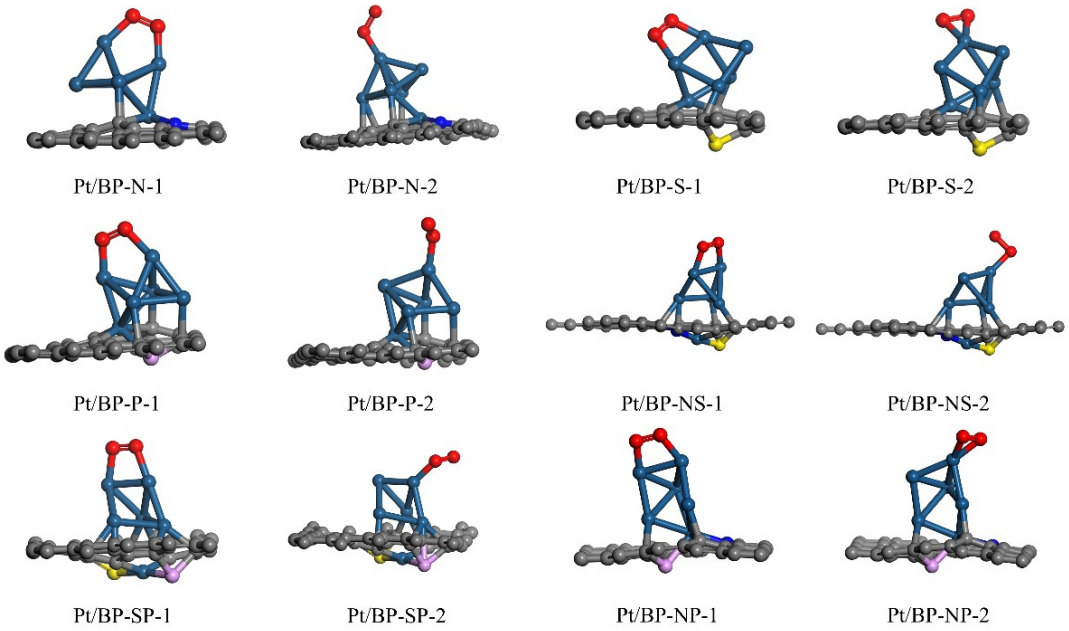

Supplementary Fig. 23 Different oxygen adsorption configurations, type 1 represents bridge oxygen adsorption, and type 2 represents apical oxygen adsorption. (Royal blue globule represents Pt atom, yellow globule represents S atom, blue globule represents N atom, pink globule represents P atom, gray globule represents C atom, red globule represents O atom)

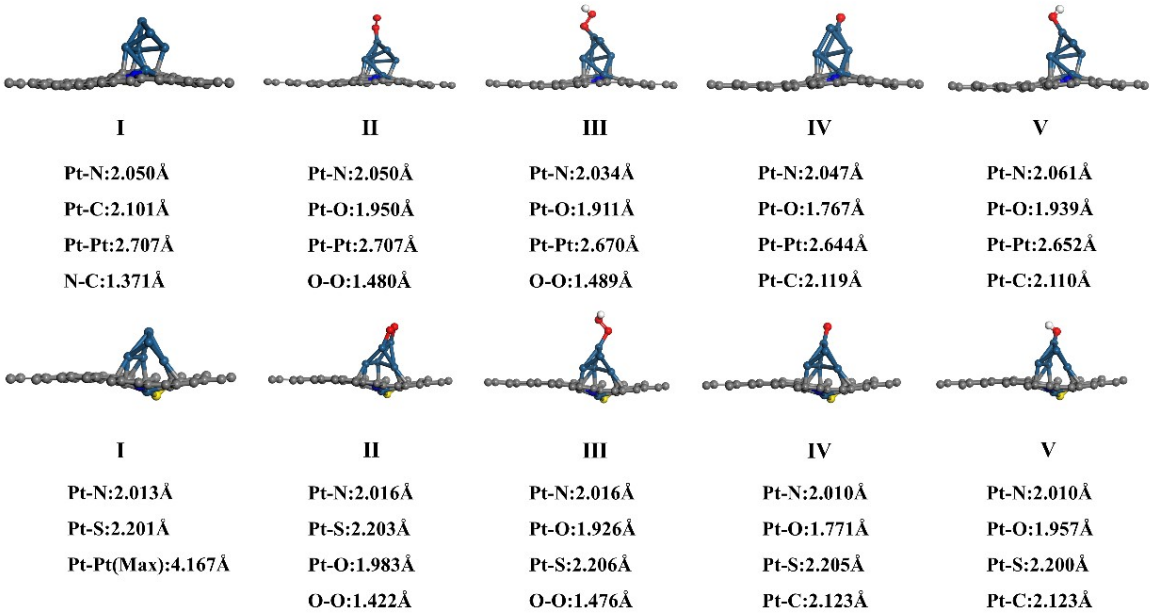

Supplementary Fig. 24 The atomic bond length of the adsorbed configuration of Pt/BP-N and Pt/BP-NS in the ORR process was counted, and only the bond length of chemisorption below 3 Å was counted. The first row is the Pt/BP-N structure, and the second row is the Pt/BP-NS structure. (Royal blue globule represents Pt atom, yellow globule represents S atom, blue globule represents N atom, gray globule represents C atom, white globule represents H atom, red globule represents O atom)

Table S1. The total DFT energy (E), corrected free energy ΔE (zero point energy (Δ E_{ZPE}), entropy multiplied by T (= 298.15 K) (TΔS)) and free energy (G) of ORR intermediates in acidic media. The energy of oxygen in it, $G(O_2) = 2G(H_2O)-2G(H_2)+4.92$.

	Pressure/bar	Temperature/K	E(DFT)/eV	ΔE/eV	G/eV
O_2	1.000	298.150	□	□	-9.975
H_2	1.000	298.150	-6.737	-0.049	-6.786
H_2O	0.035	298.150	-14.234	0.001	-14.234

Table S2. Different configurations of oxygen adsorption energy (eV), The total DFT energy (E), corrected free energy ΔE and free energy (G) of ORR intermediates in acidic media.

	E	ΔE	G
Pt/BP-N-O_2-1	-474.751	0.113	-474.637
Pt/BP-N-O_2-2	-473.947	0.021	-473.926
Pt/BP-S-O_2-1	-470.075	0.102	-469.974
Pt/BP-S-O_2-2	-469.260	0.043	-469.217
Pt/BP-P-O_2-1	-471.325	0.109	-471.216
Pt/BP-P-O_2-2	-470.363	0.037	-470.326
Pt/BP-NS-O_2-1	-470.008	0.100	-469.908
Pt/BP-NS-O_2-2	-469.562	0.015	-469.547
Pt/BP-SP-O_2-1	-465.625	0.087	-465.538
Pt/BP-SP-O_2-2	-465.470	0.039	-465.431
Pt/BP-NP-O_2-1	-470.645	0.096	-470.549
Pt/BP-NP-O_2-2	-470.470	0.032	-470.437

Table S3. The total DFT energy (E), corrected free energy ΔE (zero point energy (Δ E_{ZPE}), entropy multiplied by T (= 298.15 K) (TΔS)) free energy(G) and relative free energy (ΔG) of ORR intermediates in acidic media.

	Energy/eV	ΔE/eV	G/eV	ΔG/eV
Pt/BP-N				
U=0.00V				
O_2(g)	-462.848	0.000	-462.848	4.920
O_2*	-473.947	0.021	-473.926	3.817
OOH*	-478.392	0.299	-478.093	3.042
O*	-469.840	0.028	-469.840	0.455
OH*	-473.911	0.276	-473.634	0.054
H_2O	-462.848	0.000	-462.848	0.000
U=1.23V				
O_2(g)	-462.848	0.000	-462.848	0.000
O_2*	-473.947	0.021	-473.926	-1.103
OOH*	-478.392	0.299	-478.093	-0.648
O*	-469.840	0.028	-469.840	-2.005
OH*	-473.911	0.276	-473.634	-1.176
H_2O	-462.848	0.000	-462.848	0.000
Pt/BP-S				
U=0.00V				
O_2(g)	-457.982	0.000	-457.982	4.920
O_2*	-470.075	0.102	-469.974	2.904
OOH*	-473.549	0.331	-473.218	3.052
O*	-464.753	0.023	-464.730	0.700
OH*	-469.550	0.291	-469.258	-0.436
H_2O	-457.982	0.000	-457.982	0.000
U=1.23V				
O_2(g)	-457.982	0.000	-457.982	0.000
O_2*	-470.075	0.102	-469.974	-2.016
OOH*	-473.549	0.331	-473.218	-0.638
O*	-464.753	0.023	-464.730	-1.760
OH*	-469.550	0.291	-469.258	-1.666
H_2O	-457.982	0.000	-457.982	0.000
Pt/BP-P				
U=0.00V				
O_2(g)	-459.472	0.000	-459.472	4.920
O_2*	-471.325	0.109	-471.216	3.151
OOH*	-474.894	0.333	-474.561	3.199
O*	-465.789	0.020	-465.770	1.150
OH*	-470.596	0.264	-470.332	-0.020
H_2O	-459.472	0.000	-459.472	0.000
U=1.23V				

O_2(g)	-459.472	0.000	-459.472	0.000
O_2*	-471.325	0.109	-471.216	-1.769
OOH*	-474.894	0.333	-474.561	-0.491
O*	-465.789	0.020	-465.770	-1.310
OH*	-470.596	0.264	-470.332	-1.250
H_2O	-459.472	0.000	-459.472	0.000
Pt/BP-NS				
U=0.00V				
O_2(g)	-458.336	0.000	-458.336	4.920
O_2*	-470.008	0.100	-469.908	3.323
OOH*	-473.477	0.293	-473.184	3.440
O*	-464.620	0.013	-464.607	1.176
OH*	-469.458	0.283	-469.175	0.001
H_2O	-458.336	0.000	-458.336	0.000
U=1.23V				
O_2(g)	-458.336	0.000	-458.336	0.000
O_2*	-470.008	0.100	-469.908	-1.597
OOH*	-473.477	0.293	-473.184	-0.250
O*	-464.620	0.013	-464.607	-1.284
OH*	-469.458	0.283	-469.175	-1.229
H_2O	-458.336	0.000	-458.336	0.000
Pt/BP-SP				
U=0.00V				
O_2(g)	-454.451	0.000	-454.451	4.920
O_2*	-465.625	0.087	-465.538	3.809
OOH*	-469.620	0.293	-469.327	3.412
O*	-460.816	0.021	-460.796	1.103
OH*	-465.556	0.278	-465.279	0.013
H_2O	-454.451	0.000	-454.451	0.000
U=1.23V				
O_2(g)	-454.451	0.000	-454.451	0.000
O_2*	-465.625	0.087	-465.538	-1.111
OOH*	-469.620	0.293	-469.327	-0.278
O*	-460.816	0.021	-460.796	-1.357
OH*	-465.556	0.278	-465.279	-1.217
H_2O	-454.451	0.000	-454.451	0.000
Pt/BP-NP				
U=0.00V				
O_2(g)	-458.801	0.000	-458.801	4.920
O_2*	-470.645	0.096	-470.549	3.146
OOH*	-474.451	0.284	-474.167	2.922
O*	-465.077	0.047	-465.029	1.219
OH*	-470.527	0.293	-470.234	-0.592

H_2O				
U=1.23V				
O_2(g)	-458.801	0.000	-458.801	0.000
O_2*	-470.645	0.096	-470.549	-1.774
OOH*	-474.451	0.284	-474.167	-0.768
O*	-465.077	0.047	-465.029	-1.241
OH*	-470.527	0.293	-470.234	-1.822
H_2O	-458.801	0.000	-458.801	0.000

Table S4. The interaction energy (E_{int}) between Platinum Group and Doped substrate in Pt/BP-N(S,P). All results were in unit of eV.

	N	S	P
E_{int}	-11.391	-10.834	-10.930

Table S5. The interaction energy (E_{int}) between Platinum Group and Doped substrate in Pt/BP-NS(SP,NP). All results were in unit of eV.

	NS	SP	NP
E_{int}	-12.443	-13.248	-14.008

Table S6. The data of Pt/BP-$N_{250}S_{250}$-900-900-30% catalyst for Mass activity (A mg^{-1}) @0.9V, Specific activity (mA cm^{-2}) @0.9V, ECSA (m^2 g^{-1}), $E_{1/2}$ (V vs.RHE) of other catalysts were compared.

Catalysts	Mass activity (A mg^{-1}) @0.9V	Specific activity (mA cm^{-2}) @0.9V	ECSA (m^2 g^{-1})	Electrolyte	$E_{1/2}$ (V vs.RHE)	Ref.
Pt/BP-$N_{250}S_{250}$-900-30%	**0.149@0.8V**	**0.309@0.8V**	**48.38**	**0.5M H_2SO_4**	**0.821**	**This work**
Pt-Fe-C	0.173	0.318	-	0.5M H_2SO_4	0.76	[14]
PtCN-T120	0.252	0.434	-	0.1M $HClO_4$	0.81	[15]
Pt/NHPC-800	0.165	0.300	55.2	0.1M $HClO_4$	0.878	[16]
Pd@Pt-Co	0.232	0.110		0.1M $HClO_4$	0.86	[17]
Pt_1-N/BP	-	-	-	0.1M $HClO_4$	0.76	[18]
Pt-Ni@PtD/G	0.061	0.098	-	0.1M $HClO_4$	0.829	[19]
Cu-PtTe NTs	0.1419	0.658	21.5	0.5M H_2SO_4	0.867	[20]
Pd@Pt/NPs	0.332	0.297	112	0.1 M $HClO_4$	-	[21]
Pt/MU-MWCNT	0.1745	0.1688	103.4	0.1 M $HClO_4$	0.915	[22]

References

1 G. Kresse and J. Hafner, *Phys. Rev. B*, 1993, **47**, 558–561.

2 G. Kresse and J. Hafner, *Phys. Rev. B*, 1994, **49**, 14251–14269.

3 G. Kresse and J. Furthmüller, *Phys. Rev. B*, 1996, **54**, 11169–11186.

4 G. Kresse and J. Furthmüller, *Comput. Mater. Sci.*, 1996, **6**, 15–50.

5 P. E. Blöchl, *Phys. Rev. B*, 1994, **50**, 17953–17979.

6 G. Kresse and D. Joubert, *Phys. Rev. B*, 1999, **59**, 1758–1775.

7 J. P. Perdew, K. Burke and M. Ernzerhof, *Phys. Rev. Lett.*, 1996, **77**, 3865–3868.

8 H. J. Monkhorst and J. D. Pack, *Phys. Rev. B*, 1976, **13**, 5188–5192.

9 V. Wang, N. Xu, J.-C. Liu, G. Tang and W.-T. Geng, *Comput. Phys. Commun.*, 2021, **267**, 108033.

10 T. Lu and Q. Chen, *Comput. Theor. Chem.*, 2021, **1200**, 113249.

11 J. K. Nørskov, J. Rossmeisl, A. Logadottir, L. Lindqvist, J. R. Kitchin, T. Bligaard and H. Jónsson, *J. Phys. Chem. B*, 2004, **108**, 17886–17892.

12 V. Wang, N. Xu, J.-C. Liu, G. Tang and W.-T. Geng, *Comput. Phys. Commun.*, 2021, **267**, 108033.

13 T. Zhang, B. Zhang, Q. Peng, J. Zhou and Z. Sun, *J. Mater. Chem. A*, 2021, **9**, 433–441.

14 N. Manivannan, A. S. Kumawat and V. S. Vasantha, *Ionics (Kiel).*, 2023, **29**, 3703–3711.

15 Y. Gao, T. Uchiyama, K. Yamamoto, T. Watanabe, N. Thakur, R. Sato, T. Teranishi, H. Imai, Y. Sakurai and Y. Uchimoto, *ACS Appl. Mater. Interfaces*, 2023, **15**, 30240–30248.

16 M. Li, F. Liu, S. Pei, Z. Zhou, K. Niu, J. Wu and Y. Zhang, *Nanomaterials*, 2023, **13**, 444.

17 A. Feizabadi, J. Chen, M. N. Banis, Y. M. Yiu, L. Zhang, X. Sun and T.-K. Sham, *J. Phys. Chem. C*, 2023, **127**, 18843–18854.

18 J. Liu, M. Jiao, L. Lu, H. M. Barkholtz, Y. Li, Y. Wang, L. Jiang, Z. Wu, D. Liu, L. Zhuang, C. Ma, J. Zeng, B. Zhang, D. Su, P. Song, W. Xing, W. Xu, Y. Wang, Z. Jiang and G. Sun, *Nat. Commun.*, 2017, **8**, 15938.

19 X. Lyu, Y. Jia, X. Mao, D. Li, G. Li, L. Zhuang, X. Wang, D. Yang, Q. Wang, A. Du and X. Yao, *Adv. Mater.*, , DOI:10.1002/adma.202003493.

20 M. Dong, H. Chen, J. Xu, Z. Chen and J. Cao, *J. Alloys Compd.*, 2019, **770**, 76–81.

21 A. Pekkari, Z. Say, A. Susarrey-Arce, C. Langhammer, H. Härelind, V. Sebastian and K. Moth-Poulsen, *ACS Appl. Mater. Interfaces*, 2019, **11**, 36196–36204.

22 Q. Shu, Z. Xia, W. Wei, X. Xu, R. Sun, R. Deng, Q. Yang, H. Zhao, S. Wang and G. Sun, *ACS Appl. Energy Mater.*, 2019, **2**, 5446–5455.